Composite Structures 288 (2022) 115414

Contents lists available at ScienceDirect

Composite Structures

journal homepage: www.elsevier.com/locate/compstruct

Experimental validation of inertial twist concept for rotor blade application

Huaiyuan Gu [a,*], Javad Taghipour [b], Andres Rivero [a], Mohammadreza Amoozgar [c], Alexander D. Shaw [b], Jiaying Zhang [d], Chen Wang [e], Michael I. Friswell [b]

[a] Department of Aerospace Engineering, University of Bristol, Bristol, BS8 1TR, United Kingdom
[b] College of Engineering, Swansea University, Swansea SA2 8PP, United Kingdom
[c] Faculty of Engineering, University of Nottingham, Nottingham, NG7 2RD, United Kingdom
[d] School of Aeronautic Science and Engineering, Beihang University, Beijing, 100191, China
[e] College of Aerospace Engineering, Nanjing University of Aeronautics and Astronautics, Nanjing, 210016, China

ARTICLE INFO

Keywords:
Composite rotor blade
Morphing
Bend–twist coupling
Composite manufacturing
FE analysis

ABSTRACT

The present study performs a set of static tests to demonstrate a novel passive morphing concept. The concept introduces a bend–twist coupled composite spar to rotor blades, allowing for twist morphing to be achieved by imposing a lagwise bending moment using centrifugal forces produced by a movable mass at the blade tip. First, three composite spars are fabricated using a symmetric layup configuration with varied ply orientations. A set of static tests are designed to replicate the effect of the centrifugal forces during rotation, where the detailed distribution of twist, deflection and strain are measured on each spar with varied loading conditions. The experimental results suggest that the blade twist can be well controlled by the position of the tip mass and rotational speed. It was also found the distribution of the twist is linear when the spar deflection is small, whereas a quadratic twist distribution was observed for a large tip deflection due to the induced lateral restoring forces. Furthermore, the influence of the ply angle upon the coupled twist is demonstrated from the experimental and numerical results.

1. Introduction

Morphing blades have long been considered as an attractive solution to allow for better aerodynamic performances to be achieved [1–3]. The ability to vary the twist distribution of rotor blades in-flight is a powerful means to improve the performance of rotorcraft. A recently proposed inertial twist concept, as shown in Fig. 1, has shown great potential to be implemented in rotor blades. The concept allows for the blade to twist passively during rotation owing to the bend–twist coupling in the blade spar [4–6]. An inertial mass installed at the blade tip is moved in the chordwise direction in-flight to enable a change of the distance between the centrifugal force, and the shear centre of the spar, leading to a varied lagwise bending moment and thereby a different level of twist. In continuation of previous works, this study demonstrates the morphing concept experimentally using a set of static bending tests and provides a greater insight into how the concept will perform throughout the operational conditions.

The bend–twist coupling concept is far from new. The forward-swept aircraft, Grumman X-29, utilised bend–twist coupling in the wing design, allowing for aeroelastic tailoring which mitigated the aeroelastic divergence within the flight envelope [7]. The elastic coupling concept has also been widely exploited in wind turbine blades, where the coupling is often designed to enable the blade to passively twist towards a smaller angle of attack (twist to feather) amid gusty conditions to reduce the aerodynamic forces acting on the blade [8,9]. A similar load alleviation concept was explored by Perron [10] on commercial aircraft, where more than 20% reduction in the bending moment was achieved due to the bend–twist property possessed by the wing, leading to a significantly reduced wing weight.

A wide range of techniques have been developed in the past to obtain bend–twist properties. Many of them rely on the stiffness tailoring of the materials, which give rise to a desired anisotropic elasticity. For example the bend–twist coupling can be obtained from a thin walled rectangular composite beam fabricated with symmetric layup configurations, where the fibre orientation on two opposite walls are at the same angle to the beam span, allowing for a torque to be induced under bending loads [11–13]. Chandra et al. [14] carried out an experimental study to reveal the influence of the ply orientation upon the structural coupling, where the highest bend-induced twist was seen from the composite beam wrapped with ply angle of 45° at a given bending load. A bend–twist coupled meta-material was developed in a recently study [15], where the proposed unit cell structure comprises a cubic cell and a triangulated sub-cell along the diagonal. With this

* Corresponding author.
E-mail address: huaiyuan.gu@bristol.ac.uk (H. Gu).

https://doi.org/10.1016/j.compstruct.2022.115414
Received 13 October 2021; Received in revised form 2 February 2022; Accepted 21 February 2022
Available online 4 March 2022

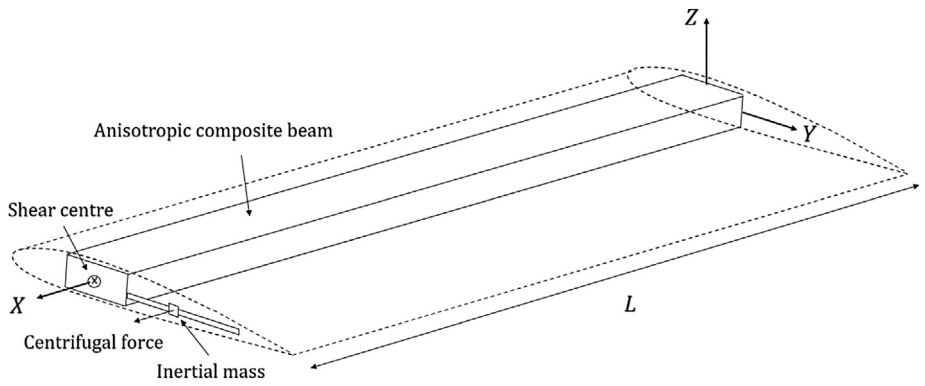

Fig. 1. Schematic representation of the inertial twist concept.

configuration, both bending and torsional stiffness can be tailored independently and the coupling properties can be effectively manipulated by changing the aspect ratio of the cells. The study showed that a more efficient coupling can be obtained from the metamaterials compared to that achieved using composites. Lobitz and Veers [16] investigated the aeroelastic stability of a helicopter blade designed with bend–twist coupling, where the relationship between the aeroelastic boundary and coupling coefficient was revealed. In general, an increase in the magnitude of the coupling coefficient was detrimental to the stability which could either cause reduced flutter or divergence speeds depending on the direction of the induced twist. However, for both positive (twist towards stall) or negative (twist towards feather) coupling coefficient, very high limits of the rotor speeds were predicted compared to the designed rotating speed, when the coupling coefficients were less than 0.8.

Smart materials have long been considered as strong candidates for morphing blades which may be embedded into structures and thereby reduce the complexity of the actuation systems [17–19]. For example shape memory alloys (SMA) allow the morphing to be driven thermally as a result of the phase change of the material under different temperatures [20,21]. Ameduri and Concilio [22] achieved active blade twist in a rotor blade by implementing an SMA pre-twisted tube which transmitted rotation to the blade during the strain recovery process, leading to a desired twist distribution. However, the frequency of the response is relatively low due to the speed of heat transfer [23]. Moreover the cyclic heating and cooling may cause the structure to be susceptible to fatigue. Piezoelectric materials can be deformed by electric charge, and have been applied extensively in morphing concepts. They are most widely made into thin sheets which can be attached to the structures to generate a local strain field on the surfaces [24]. Chen and Chopra [25] demonstrated the possibility of twisting a rotor blade by embedding an array of equally spaced piezoelectric patches on both top and bottom surfaces of the blade at an positive and negative angle respectively. Less than 0.5° of twist was observed due to the rigidity of the structure and the limitations of the torque produced from the piezoelectric patches.

In this work, an experimental study is performed to demonstrate the inertial twist concept using a set of static bending tests and three composite spars manufactured with different ply angles. This paper is arranged as follows. First, the detailed spar manufacturing process is described including the tooling, layup and curing processes. Then the experiment configuration is presented followed by a description of the finite element (FE) models. Finally, the measured results are compared with the FE predictions and the key aspects that determine the effectiveness of the morphing concept are discussed.

2. Spar manufacturing

To demonstrate the morphing concept, three thin-walled rectangular spars were fabricated with Hexcel 8552/IM7 unidirectional carbon fibre prepreg. Three different ply angles were used, namely 20°, 30° and 45°. The spars were manufactured by wrapping the pre-cut laminate onto rectangular foam cores in a way that the layup on two opposite walls were mirror images with respect to the symmetric plane of the section to obtain the bend–twist coupling, as shown in Fig. 2 and Table 1. The spars were then placed into an autoclave for curing, and the detailed curing process is described in the following sections. Finally, a set of pin holes was drilled at both ends of the spars, allowing them to be connected to the fixtures.

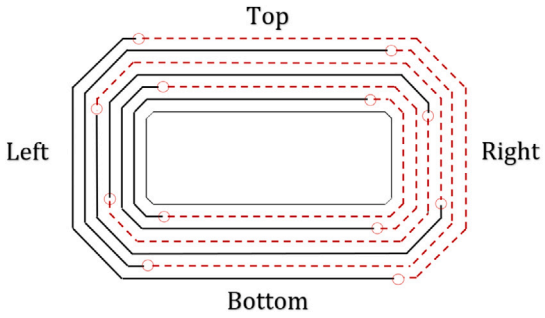

Fig. 2. Lay-up configuration in a cross-section of spars: black solid lines and red dashed lines represent plies cut in $\theta°$ and $-\theta°$ directions respectively.

2.1. Foam core cutting

Three rectangular foam cores with a length of 1100 mm were cut from a Rohacell foam sheet (110 XT-HT) which is able to resist a 7 bar pressure at 190 °C, sufficient to withstand the required curing conditions of the prepreg. A 1 mm chamfer was introduced at each corner to avoid ply bridging during the layup process as shown in Fig. 3. The foam core was cut with tapered regions at both ends, preparing for the thickness tapering in the layup, described in Section 2.2. The taper angle was designed to mitigate the stress concentration caused by the ply drops.

2.2. Layup

The unidirectional carbon fibre prepreg was cut into the required sizes and wrapped onto the Rohacell rectangular foam bars. Note that the ply joints were staggered around the corners to avoid fibre rich areas as shown in Fig. 2. A vacuum pump was used after laying every two plies to remove air pockets that were trapped in the laminates. Pin areas were designed at both ends of the spars where the reinforcements plies were essential to increase the local tensile strength. A set of 0° and 90° plies were embedded in the laminate in the pin area, leading to a tapered layup configuration. One ply was dropped in each step and the distance between each ply drop (stagger) was 6 mm, as shown in Fig. 4, to mitigate the local stress concentration [26].

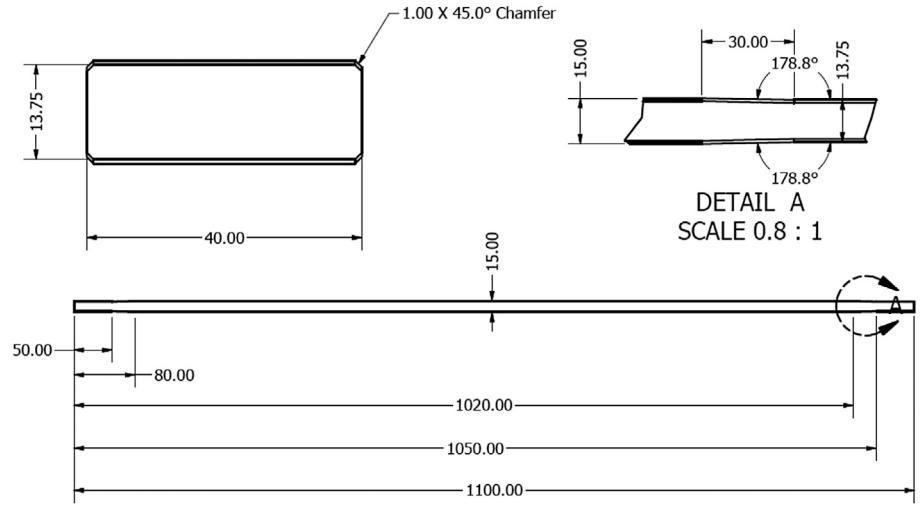

Fig. 3. Dimensions of the foam core.

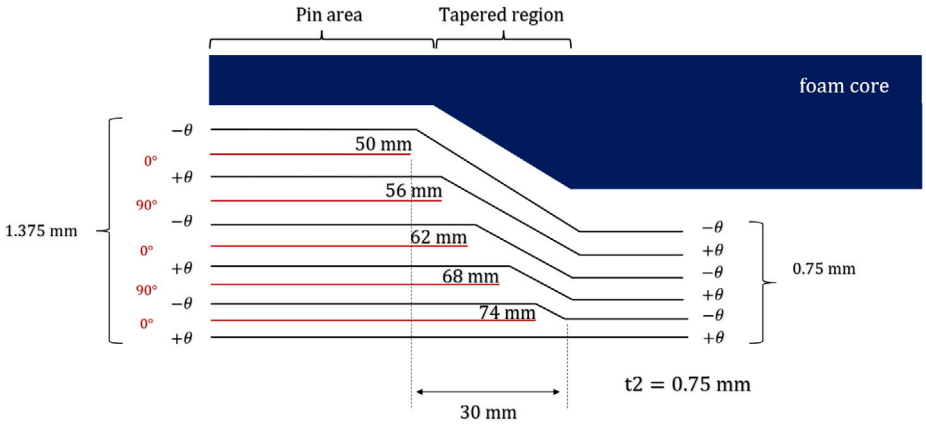

Fig. 4. Schematic representation of the layup configuration at the pin area and tapered region.

Table 1
Layup configurations of the spars.

Spar config.	Top wall	Bottom wall	Left wall	Right wall
20°	$[+20°/-20°]_3$	$[+20°/-20°]_3$	$[20°]_6$	$[20°]_6$
30°	$[+30°/-30°]_3$	$[+30°/-30°]_3$	$[30°]_6$	$[30°]_6$
45°	$[+45°/-45°]_3$	$[+45°/-45°]_3$	$[45°]_6$	$[45°]_6$

2.3. Curing

After the layup process, each spar was wrapped in R210 unperforated prepreg release film, as shown in Fig. 5(a). Cork dams were placed at both ends of the tooling to prevent resin bleeding, and ensure that the fibre volume fraction is preserved during the curing process. The spars were then wrapped by two breather layers shown in Fig. 5(b), and placed inside an envelope vacuum bag, as shown in Fig. 5(c) with two valves. The quality of the vacuum bag was checked by verifying that the bag was able to hold a vacuum pressure of −2 bar for 20 min without being connected to a vacuum pump shown in Fig. 5(d). The vacuum bag was then taped to a steel tooling plate to prevent it from moving when under autoclave pressure.

The curing cycle was set following the 8552/IM7 data sheets i.e. 180 °C, with 7 bar of autoclave pressure and 1 bar of pressure inside the vacuum bag, as shown in Fig. 6. The cure condition was monitored by using four thermocouples at four different locations in the vacuum bag, and both autoclave pressure and vacuum bag pressure were recorded for quality control purposes. After the curing process, the deflections of the spars were measured to assess the quality of the manufacturing. A small mount of flapwise deformation was noticed in each spar, as shown in Fig. 7, which was most likely caused by loads that occurred during the curing processes, e.g. thermal stresses and pressure loads. It can be seen that the deformation was more obvious in the spar fabricated with higher ply angles, which was attributed to their inherent low bending stiffness, which made them more susceptible to the loads applied during manufacturing particularly under the curing temperature.

3. Experiment

3.1. Bending test

A set of static bending tests was undertaken to demonstrate the inertial twist concept, and more specifically the test aimed to predict the twist that can be achieved from the rotating composite spars equipped with a tip fixture and movable mass. The experimental configuration is illustrated in Fig. 8. The root of the spar was clamped to a rigid end fixture made of 8 mm thick steel plates to ensue sufficient rigidity and strength. The tip of the spar was connected to a pair of T-shaped tip fixtures cut from 3 mm Aluminium 7075 sheets, which provided high yield strength, with low density to minimise flapwise bending moment caused by the weight of the tip fixture. An array of pin holes were cut along the tip fixture, allowing tip loads to be applied at

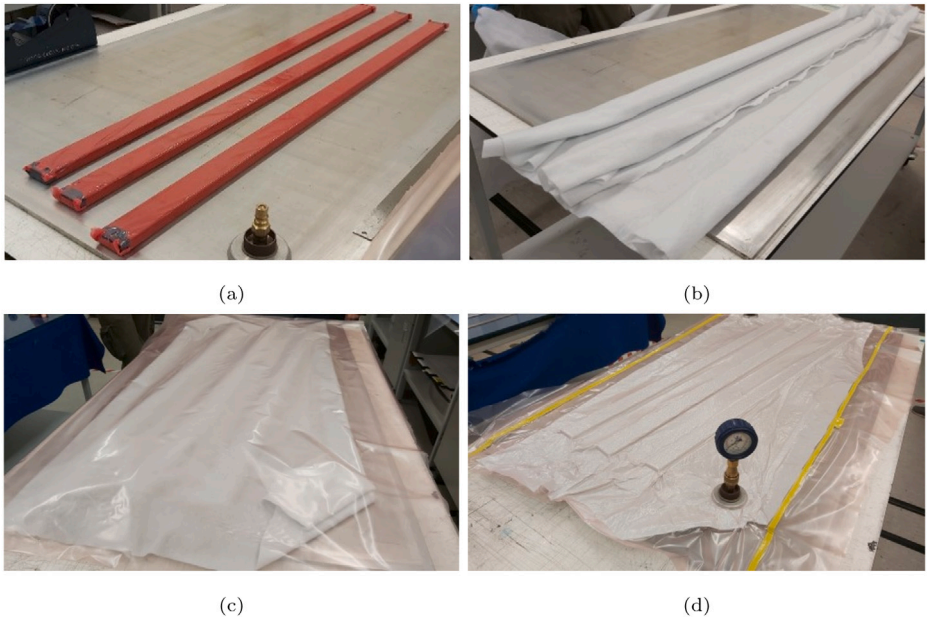

Fig. 5. Vacuum bagging process (a) spars wrapped in prepreg release film; (b) spars wrapped in two breather layers; (c) the envelope vacuum bag for curing; (d) sealed vacuum bag undergoing a vacuum test.

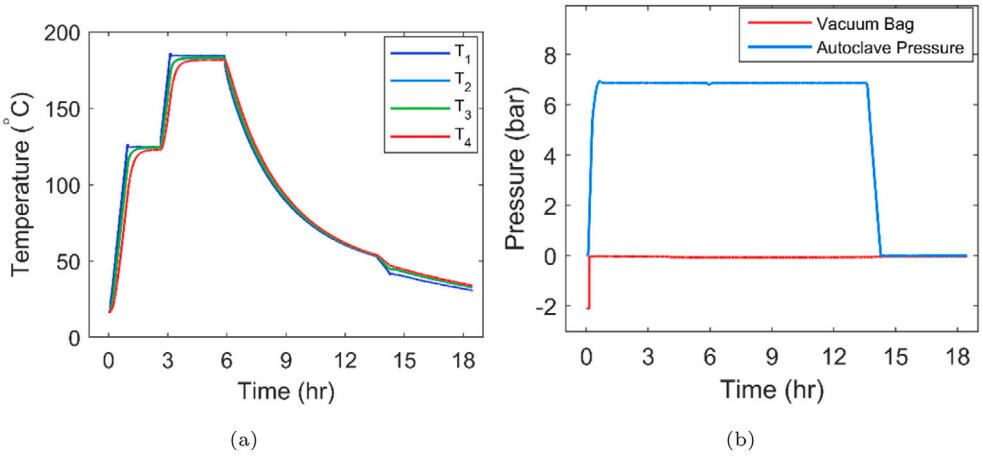

Fig. 6. Cure cycle temperature and pressure set for the composite spars.

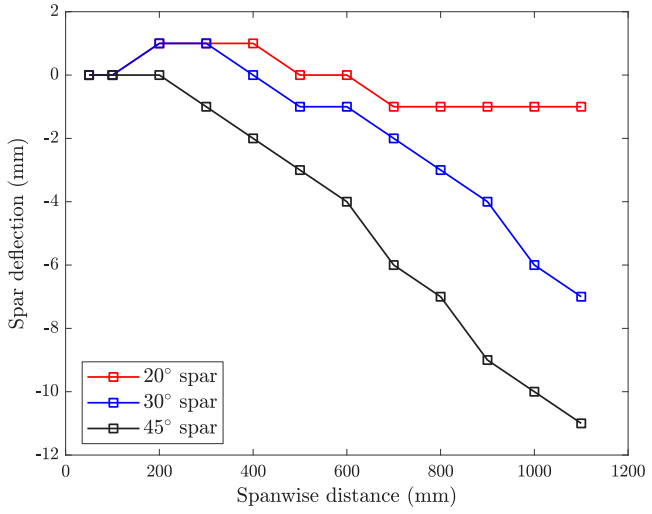

Fig. 7. Initial flapwise deflection of the spars measured after manufacturing processes.

different chordwise positions and the off-set displacement, y_d, ranged from −100 mm to 100 mm.

For this preliminary demonstration, only the effect of centrifugal forces were considered in the test, whereas the influences of aerodynamic forces e.g. lift and drag were out of the scope of the current study. The centrifugal forces were modelled using a pair of pulling forces applied in the axial direction of the spars, i.e. F_a and F_b, shown in Fig. 9, simulating the centrifugal forces caused by the tip fixture and the movable mass respectively. The tip fixtures were connected to two cables, i.e. cable A and cable B shown in Fig. 8, and the pulling forces were applied by hanging weights at the free end of each cable. Both the tip fixture and movable mass were 150 g, and therefore weights of 10 kg, 20 kg and 40 kg were applied to each cable to replicate the centrifugal forces on the spars under rotational speeds of 240, 340 and 480 rpm, (see Fig. 11).

Two sets of tests were carried out to predict the twist of the spar under various rotational speeds and mass positions. In the first test, both cables were connected to fixed positions on the tip fixture, while the twist was measured with various weights hung to the cables to simulate the centrifugal forces caused by different rotational speeds.

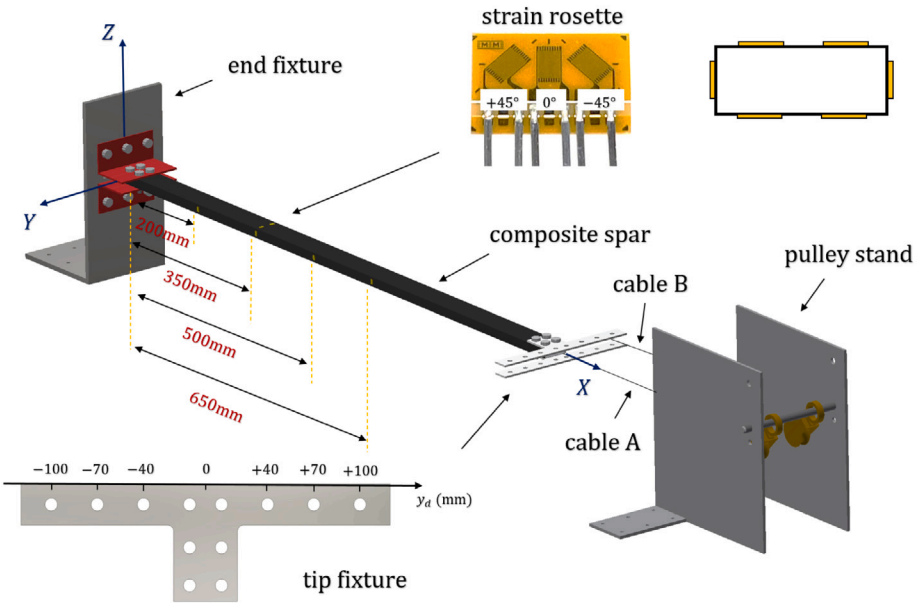

Fig. 8. Configuration of the static bending test.

Fig. 9. Elevated view of the test configuration and the pulling forces applied to the tip fixture.

The second test considered the spars rotating at a constant rotational speed, but with different mass positions. Therefore a constant weight was hung to the cables, and cable B moved from $y_d = -100$ mm to $y_d = 100$ mm on the tip fixture, as shown in Fig. 8.

Rectangular strain rosettes were installed on each spar, allowing both the axial and shear strain to be measured during each test. Each strain rosette contains three measuring grids oriented at 0°, +45° and −45°. The true axial strain can be obtained from the 0° grid, whereas the true shear strain, γ, can be calculated from the readings obtained from the +45° and −45° grids as,

$$\gamma = \frac{\varepsilon_{45°} - \varepsilon_{-45°}}{2} \tag{1}$$

Four strain rosettes were installed to one of the side walls as shown in Fig. 8. At the position $X = 350$ mm, strain rosettes were placed on all sides of the spar to obtain the strain distribution along the chord. The twist and deflection of the spars were measured using Omron laser sensors ZX2-LD 100, with measurement range 100 ± 35 mm and resolution 5 μm. When measuring the bending deflection, a single laser sensor was placed approximately 100 mm from the side wall as shown in Fig. 10(a). To measure the twist, a foam strip was first mounted to the spar and a pair of laser sensors were then installed above the top surface. The twist was determined by calculating the differences between the vertical displacements measured at both ends of the foam strip,

$$\phi = \frac{d_1 - d_2}{L_s} \tag{2}$$

where d_1 and d_2 are the vertical displacements measured from both ends of the foam strip. L_s is the horizontal spacing between the two laser sensors. The measurement was repeated at 7 different locations along the span for each load case to obtain the distribution of the deflection and twist.

3.2. FE modelling

Finite element analysis (FEA) was performed using the commercial package ABAQUS 2017 to provide numerical predictions. The model configurations are shown in Fig. 12, and the spars and tip fixture were modelled using 3D shell elements corresponding to element code S4R in ABAQUS. Initial curvatures were introduced to each spar model based on the measurements shown in Fig. 7. Forty thousand elements were included in the spar model to ensure mesh independence of the results. The material properties of the laminate were chosen based on the data sheets of Hexcel 8552/IM7 which are listed in Table 2. The tip fixture model was assumed to be rigid and connected to the spar models using tie constraints in Abaqus. This constraint allows the surfaces of the pin area on the spar model to have equal displacements to the tip fixture, simulating the conditions of the experiment.

Note that in the test configuration, the directions of the pulling forces were pointing towards the position of the pulley wheels, which were at an angle, α, to the orientation of the tip fixture after the spars were deflected, as illustrated in Fig. 13(a). The induced angle resulted in lateral components F_{ra} and F_{rb} of the pulling forces, leading to restoring bending moments, and thereby reduced twist. The influence of the restoring forces on the inertial twist concept has also been reported in the literature [4]. Under rotational conditions, the directions of the centrifugal forces were determined by the positions of the centre of rotation and the movable mass at the spar tip, which was at an angle, α_c, to the spar axial direction leading to a restoring force, F_{cr}, and therefore a reduced bending moment will be applied to the blade, as illustrated in Fig. 13(b). Similar to the static configuration used in this study shown in Fig. 13(a), the restoring forces, F_{cr}, caused by centrifugal forces increase with tip loads due to an increase in the lateral component of the centrifugal force, F_c. The restoring forces that occurred in the static tests might have different magnitudes compared to those caused by centrifugal forces during rotation, as the deflection

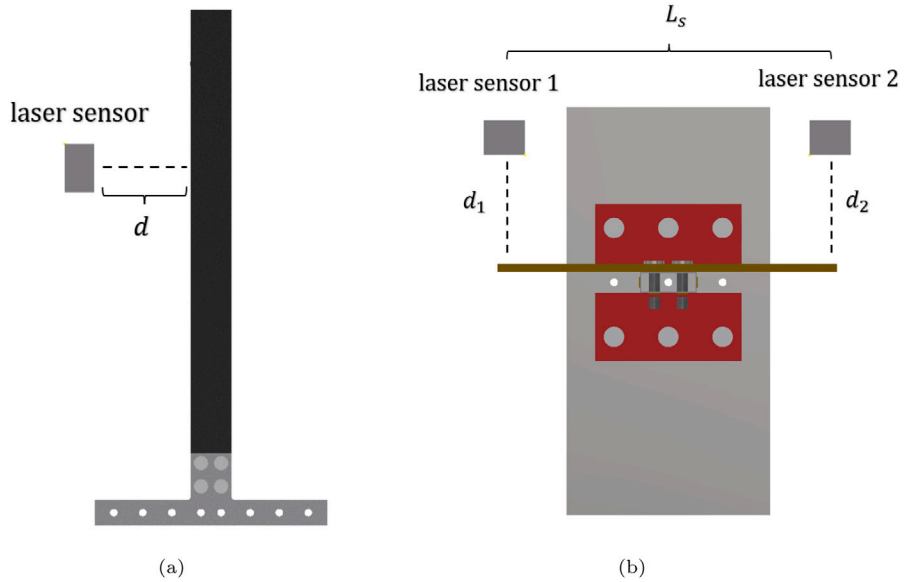

Fig. 10. Sensor configurations for the measurement of (a) bending deflection and (b) twist.

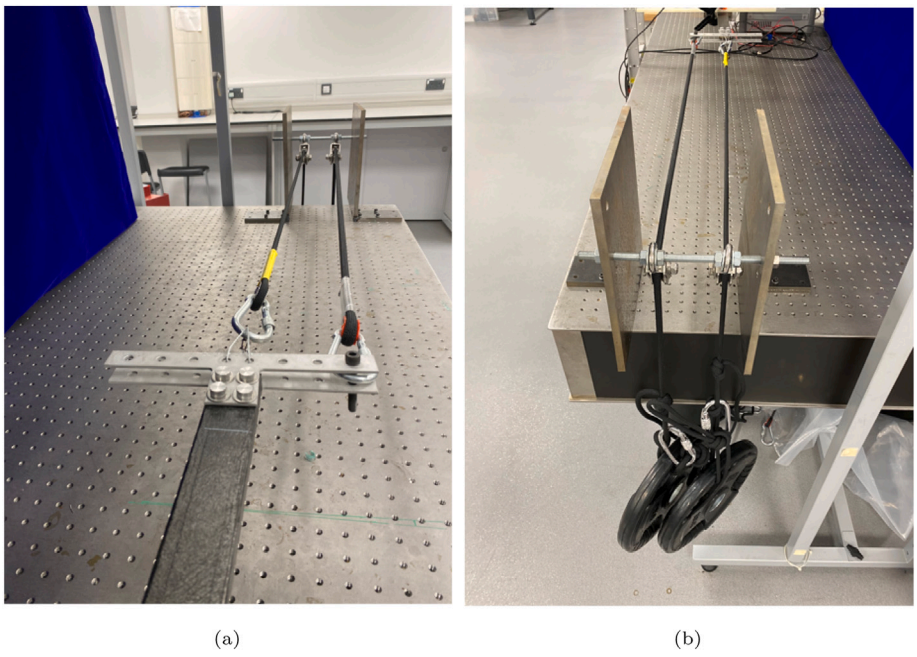

Fig. 11. Load condition applied in the experiment.

angles α_c is related to the spar length, L_0, whereas α_c is affected by the distance between the spar tip and the pulley wheels, L. This is one of the fundamental limitations of using static test configuration to replicate the actual rotational conditions. With a small angle approximation, the magnitude of the restoring forces, F_{ri}, that occurred in the static tests can be related to the tip deflection of the spars, d_{tip}, as,

$$F_{ri} = F_i \sin(\frac{d_{tip}}{L}) \approx F_i \frac{d_{tip}}{L} \quad (i = a, b) \tag{3}$$

It is clear that the restoring force is proportional to pulling forces F_i and tip deflection, d_{tip}, and inversely proportional to the distance between the spar tip to the pulley wheels, L. Hence the effect of the restoring forces can be modelled using a linear spring element with stiffness of F_i/L attached to the model as shown in Fig. 12.

Table 2
The material properties used in the spar model.

E_{11} (GPa)	E_{22} (GPa)	G_{12} (GPa)	υ_{12}	ρ
154	8.9	5.3	0.32	1400

4. Results

Figs. 14 and 15 present the distributions of the bending deflections and twist measured from the spars subjected to tip loadings of 10 kg, 20 kg and 40 kg. It is clear that both the bending deflection and twist increased with the applied weights. It was found that the twist increased linearly along the spar when the weight was small, whereas the twist turned into quadratic forms with increasing tip loads. This was associated with the restoring forces as described in Section 3.2.

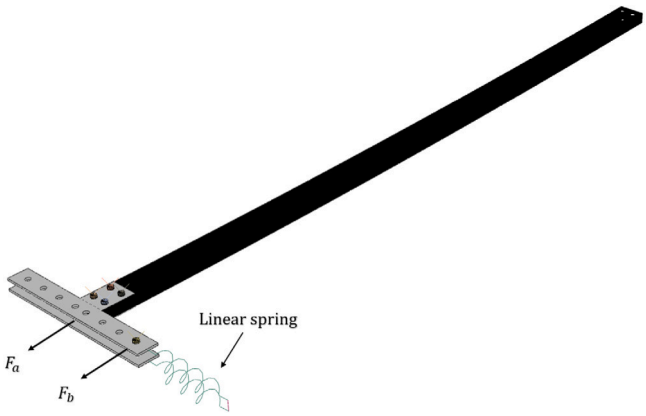

Fig. 12. FE model configurations.

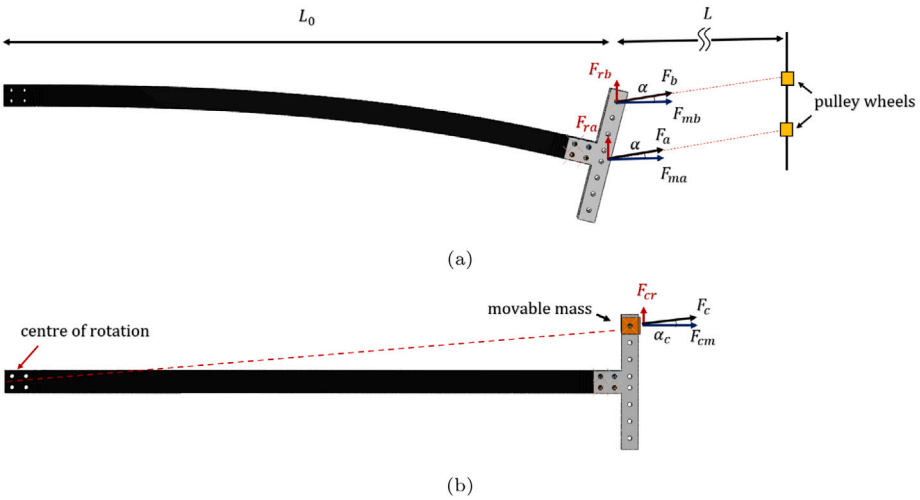

Fig. 13. Comparison of (a) the pulling forces applied to the spars in the static test and (b) centrifugal forces occur under rotating conditions.

The magnitude of the lateral components(restoring forces) were proportional to the applied loads, which led to a significant bending moment, M_r, produced in the opposite direction to that generated by the pulling forces. The magnitude of the bending moment, M_r, can be expressed as,

$$M_r = F_r L_0 (1 - \frac{X}{L_0}) \tag{4}$$

The overall bending moment along the spar can be expressed as,

$$M_F - M_r = y_d F_{mb} - F_r L_0 (1 - \frac{X}{L_0}) \tag{5}$$

With the presence of the restoring force, the bending moment introduced by the pulling forces increased linearly from the root to tip of the spars. The larger the restoring force, the greater slope will occur in the distribution of the bending moment. The linear distribution of the bending moment was also reflected in the strain distributions, as shown in Figs. 16 and 17. It can be seen that the measured axial and shear strain increases linearly along the span when the applied load was large. Furthermore the gradient of the strain distribution increased with the weight due to the increase in the bending deflections and restoring forces.

The solid curves shown in the Figs. 14 to 17 represent the numerical results given from the FE analysis. In general, the FE predictions agreed reasonably well with the experimental data particularly for small tip loadings i.e. 10 kg and 20 kg, and the discrepancies were mainly caused by a slight misalignment between the cable and spar axial directions due to the complex initial curvatures existed in the spars shown in Fig. 7, leading to a small difference between the directions of the forces applied to the models and real samples. Furthermore, when large deflections occurred in the spars, an increased discrepancy was observed between the numerical results and measured data, which was attributed to the geometric non-linear effect. More specifically, when the deviation angle, α, was large, the reduction in the longitudinal component of the pulling force, F_{mb}, shown in Fig. 13(a), became significant and the effect was not considered in the linear FE model.

Figs. 18(a) and (b) present the comparison of the measured bending deflections and twists from the three spars subjected to a tip load of 40 kg. The maximum deflection was measured from the 45° spar, while its twist was found to be the minimum. This was likely attributed to the large restoring forces that occurred on the spar. It can be seen that the highest slope of the axial strain distribution was observed on the 45° spar, as shown in Fig. 18(c), indicating the restoring force acting on the 45° spar was greater than that on the 20° and 30° spars. The results also suggested that the 20° spar offered the maximum twist and the minimum bending deflection. To further interpreter the results, the measured shear strains were normalised by the axial strains, as shown in Fig. 19. The results indicate that the 20° spar produced the highest shear strain for a given axial strain, and therefore it was able to offer the highest twist at a given bending curvature. This phenomenon was consistent with the conclusions drawn from the existing studies [5,13].

Fig. 20 shows the tip twist measured from the spars subjected to a loading of 20 kg while cable B was connected to the various positions on the tip fixture from $y_d = -100$ mm to $y_d = 100$ mm, as shown in Fig. 8. It was found that the tip twist changed almost linearly with

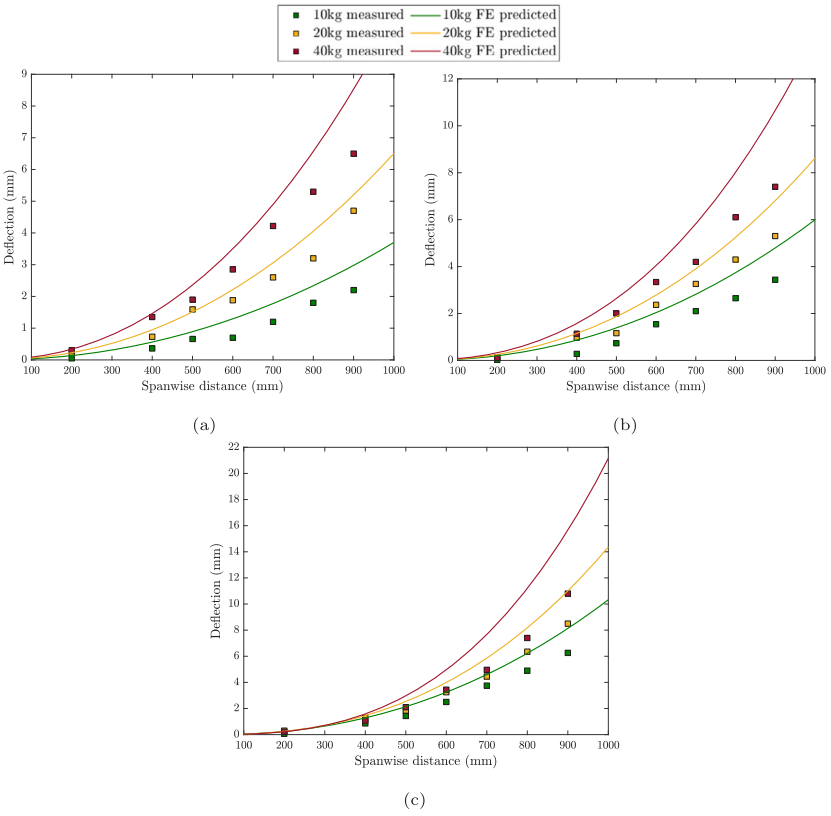

Fig. 14. Deflection of the spars fabricated with various ply orientations (a) 20° (b) 30°, and (c) 45°.

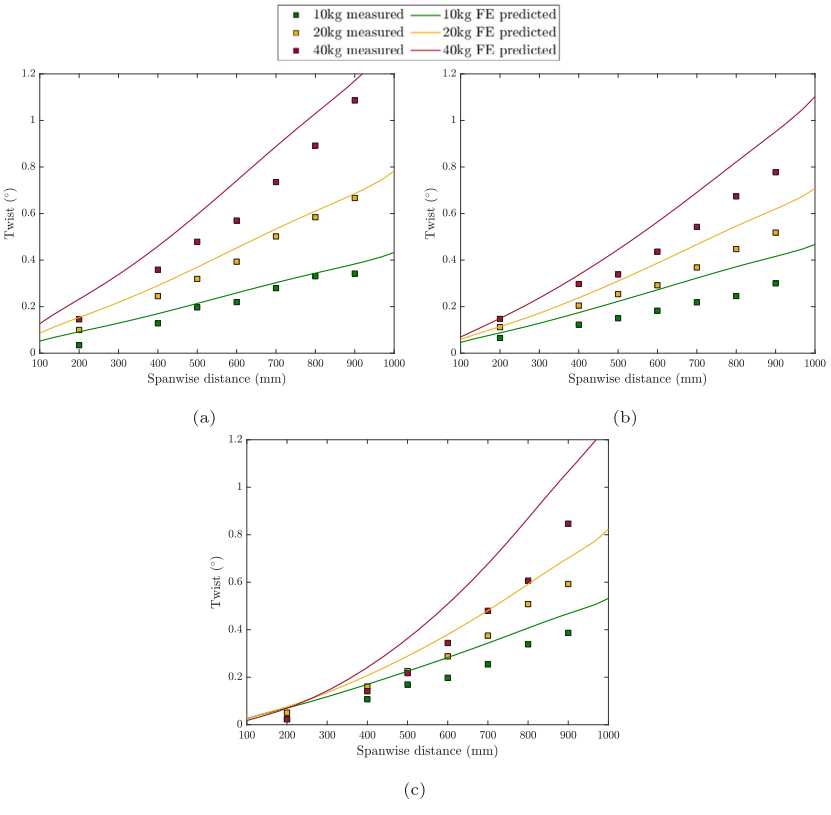

Fig. 15. Twist of the spars fabricated with various ply orientations (a) 20° (b) 30°, and (c) 45°.

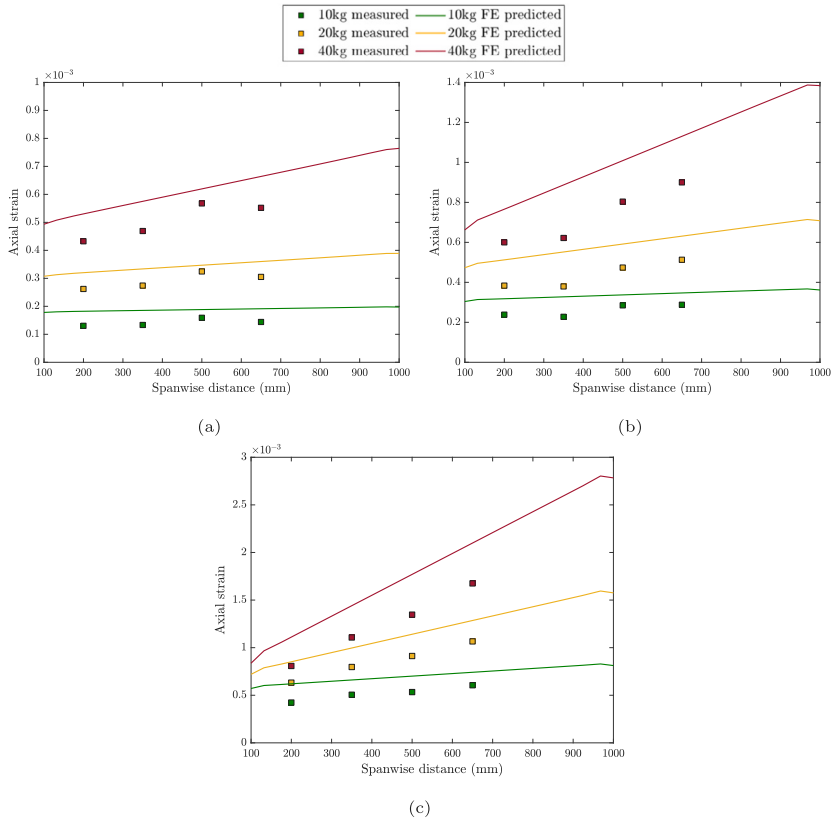

Fig. 16. Spanwise distribution of the axial strain on the spars fabricated with various ply orientations (a) 20° (b) 30°, and (c) 45°.

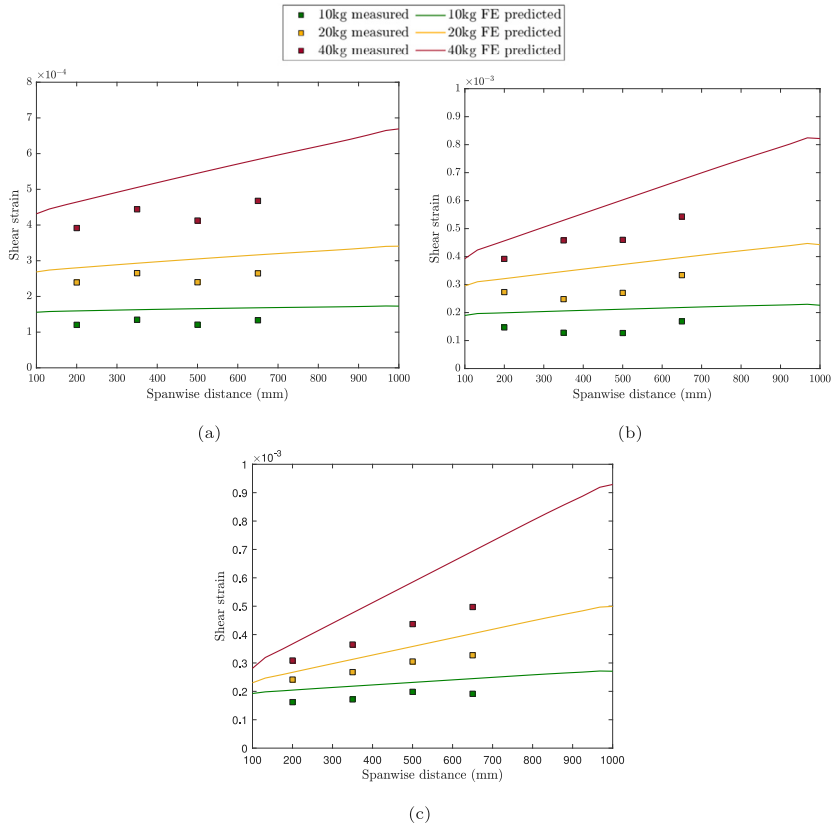

Fig. 17. Spanwise distribution of the shear strain on the spars fabricated with various ply orientations (a) 20° (b) 30°, and (c) 45°.

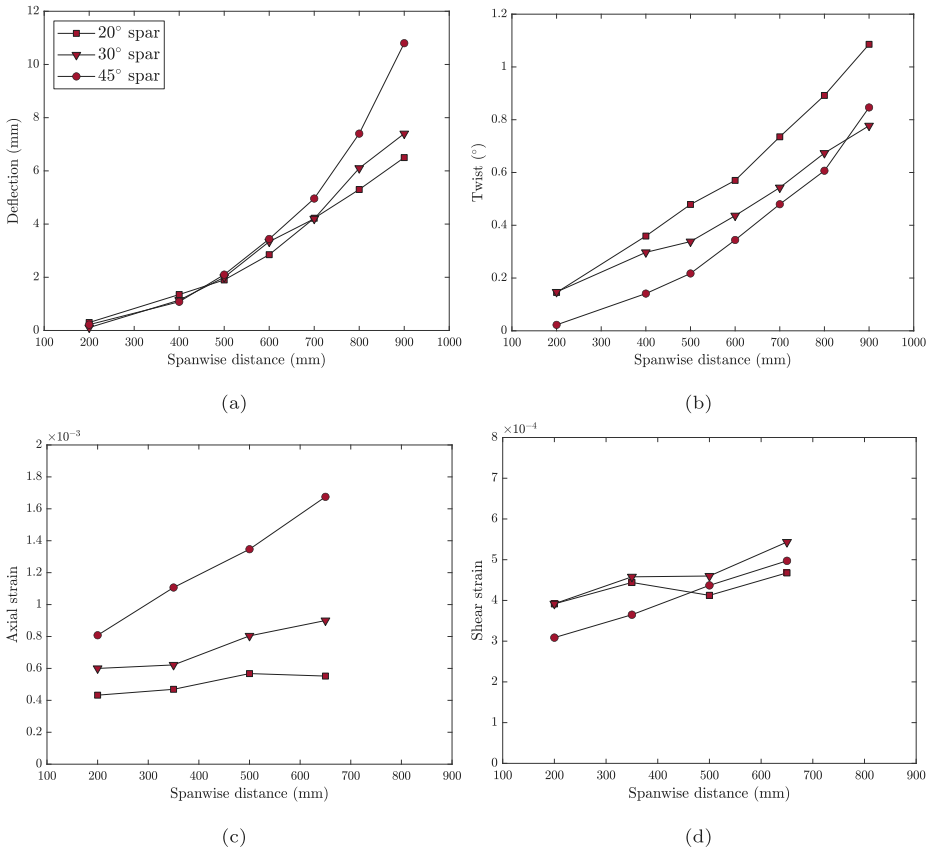

Fig. 18. Comparison of the (a)bending deflection, (b)twist, (c) axial strain (d) shear strain of the spars fabricated with various ply orientations subjected to a tip load of 40 kg.

y_d for each spar. Fig. 21 shows the measured strain distribution along the spanwise and chordwise directions for the 20° spar for various loading positions, and very similar plots can be obtained for the 30° and 45° spars. It was clear that both axial and shear strain along the span increased with y_d due to the increase in the applied bending moment. As expected, the slope of the axial strain distribution along the chordwise direction also increased with y_d. Note the axial strain measured from both sides, where $Y = -20$ mm and $Y = 20$ mm, were not equal due to the presence of the pulling force, F_a, applied at the centre the fixture, as shown in Fig. 8. The shear strain measured from the side walls (left and right) were significantly higher than that measured from the top and bottom walls, which was attributed to the extension-shear coupling property possessed by the laminates, whereas the layup configurations of the top and bottom walls were quasi-isotropic and therefore, no obvious coupling effect was seen from the experiment.

5. Discussion

The experimental results have shown that the induced restoring force, F_r, caused a significant effect on the angle of twist. To further demonstrate the influence of the restoring forces, a set of FE analyses were performed to compare the induced tip twist on the spar models with and without the presence of the restoring forces, F_r, (by setting the stiffness of the lateral spring as shown in Fig. 12 to zero). The obtained results are shown in Fig. 22. It was found that without the restoring force, F_r, the tip twist increased linearly with applied weights. The maximum tip twist was observed on the model created with a ply angle of 45°, while the 20° model exhibited the minimum twist. However, when F_r was introduced to the spar models, as shown by the dotted lines, the tip twists were remarkably reduced, particularly in the 30° and 45° models, due to their large bending deflections. The 20° model exhibited the minimum bending deflection at the tip which led to a relatively smaller F_r, compared to that in the 30° and 45° models and thereby produced the highest twist especially when the applied weight was large.

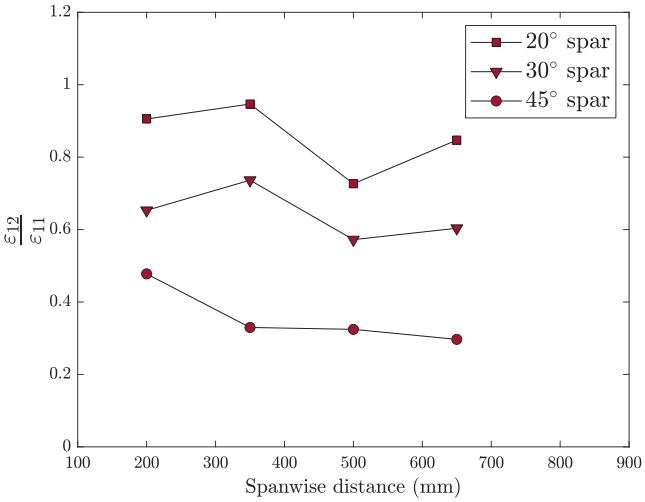

Fig. 19. Comparison of the ratio between the induced shear strain and axial strain among the three spars.

Fig. 23 shows the twist of the spar models created with various layup orientations subjected to a constant tip load of 40 kg, where the restoring forces were assumed to be zero. It was found that without the presence of restoring forces, the twist increases with ply angles. A high ply angle is therefore recommended for the inertial twist application when the restoring forces are small i.e. the centrifugal forces produced by the tip mass align well with the spar axis. In practice, this can be

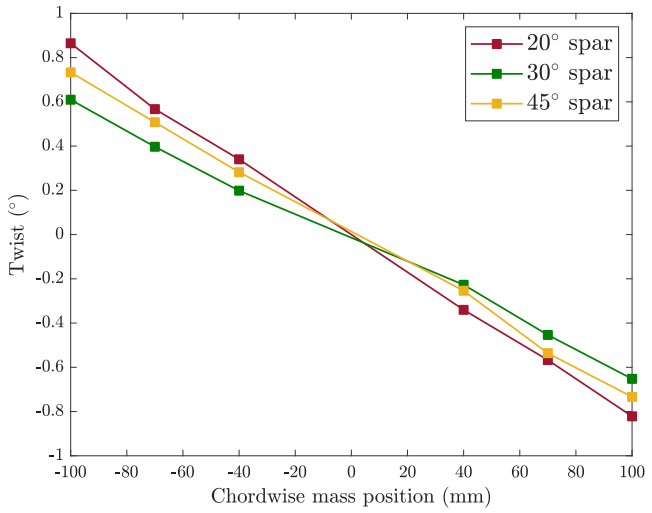

Fig. 20. Measured tip twist of the spars subjected to a loading of 20 kg placed as the chordwise position varies.

achieved by either increasing the length of the spar or reducing the offset displacement, y_d, as shown in Figs. 8 and 13.

To validate the conclusion, a simple beam analysis was conducted to demonstrate the effect of the ply angle on the inertial twist concept. The bend–twist properties possessed in composite spars are often represented by a linear equation where the bending moment, M_z, and torque, T_x are related to the rate of twist, ϕ'_x, and bending curvature, k_z, through a 2 by 2 stiffness matrix,

$$\begin{bmatrix} T_x \\ M_z \end{bmatrix} = \begin{bmatrix} \overline{GJ} & -g \\ -g & \overline{EI} \end{bmatrix} \begin{bmatrix} \phi'_x \\ k_z \end{bmatrix} \tag{6}$$

Hence the rate of twist and bending curvature produced by a given loading can be obtained by the inverse of Eq. (6),

$$\begin{bmatrix} \phi'_x \\ k_z \end{bmatrix} = \frac{1}{\overline{GJ}\ \overline{EI} - g^2} \begin{bmatrix} \overline{EI} & -g \\ -g & \overline{GJ} \end{bmatrix} \begin{bmatrix} T_x \\ M_z \end{bmatrix} \tag{7}$$

From Eq. (7), the rate of twist can be associated to the applied bending moment, M_z, as,

$$\phi' = \alpha M_z \tag{8}$$

where

$$\alpha = \frac{g}{\overline{GJ}\ \overline{EI} - g^2} \tag{9}$$

Hence, the magnitude of the twist produced by a given bending moment is proportionate to α. The greater the magnitude of α, the smaller the bending moment that is needed to produce a targeted twist, and in practice that indicates a smaller actuation force is required.

A variational-asymptotic beam cross-sectional (VABS) analysis was performed to determine the stiffness matrix shown in Eq. (6), for spar models with various ply orientations and thereby to determine the values of α. The methodology was developed by Hodges and his co-workers, and widely used for anisotropic beam studies due to its low computational effort. The analysis splits the three-dimensional beam analysis into a two-dimensional cross sectional analysis and one dimensional beam analysis, and the values in the stiffness matrix were calculated based on the predefined warping functions and corresponding strain energy within the beam cross section [27,28]. The evaluated $\overline{EI}$, $\overline{GJ}$ and g are given in Table 3, and the calculated α is plotted in Fig. 23. The α increases with ply orientation and reaches the maximum value around 40° which agreed well with the conclusion drawn from the FE results.

Table 3
Calculated elements included in the stiffness matrix.

Ply orientation	Bending rigidity, $\overline{EI}$ (N m^2)	Torsional rigidity, $\overline{GJ}$ (N m^2)	Coupling term, g (N m^2)
0°	2810	59.3	0
5°	2600	70.6	64.7
10°	2200	103	123
15°	1800	150	169
20°	1420	200	194
25°	1060	247	197
30°	775	277	181
35°	562	287	152
40°	416	280	120
45°	320	260	89

6. Concluding remarks

In the present study, the inertial twist morphing concept has been demonstrated using a set of simplified static bending tests. The composite spars fabricated with various ply angles were tested, and the detailed distributions of the twist, bending deflection and strain were measured for a range of loads and load positions. The experimental results show that the twist in the spars can be well controlled by the magnitude and chordwise positions of the loads. Furthermore, reasonable levels of twists were measured from the tests and a good agreement has been achieved between the measured data and the numerical predictions.

The presence of the restoring forces, F_r, introduced by the bending deflection were noticed in the static test configuration, which led to a significant reduction in the twist. A similar effect can also be seen from the spar subjected to rotational conditions due to the lateral component of centrifugal forces [4]. It was found that the influence of the restoring force is related to ply angles of the spars. The twist of the spar created with low ply angle is relatively insensitive to the presence of the restoring forces. It shows that when the restoring forces were significant, the highest twist was obtained from the spar fabricated with 20° ply angle, whereas the 40° spar model offers the most efficient bend–twist property when the restoring forces are zero. However, it is still unclear what the impact of aerodynamic forces on the inertial twist concept will be, which is the next step of the study.

CRediT authorship contribution statement

Huaiyuan Gu: Conceptualization, Methodology, Formal analysis, Investigation, Writing – original draft. **Javad Taghipour:** Investigation, Writing – review & editing. **Andres Rivero:** Investigation, Writing – review & editing. **Mohammadreza Amoozgar:** Writing – review & editing. **Alexander D. Shaw:** Supervision, Project administration, Writing – review & editing. **Jiaying Zhang:** Writing – review & editing. **Chen Wang:** Writing – review & editing. **Michael I. Friswell:** Supervision, Project administration, Writing – review & editing.

Declaration of competing interest

The authors declare that they have no known competing financial interests or personal relationships that could have appeared to influence the work reported in this paper.

Acknowledgement

The authors acknowledge funding from the European Union's Horizon 2020 project 'Shape Adaptive Blades for Rotorcraft Efficiency (SABRE)', under grant agreement 723491.

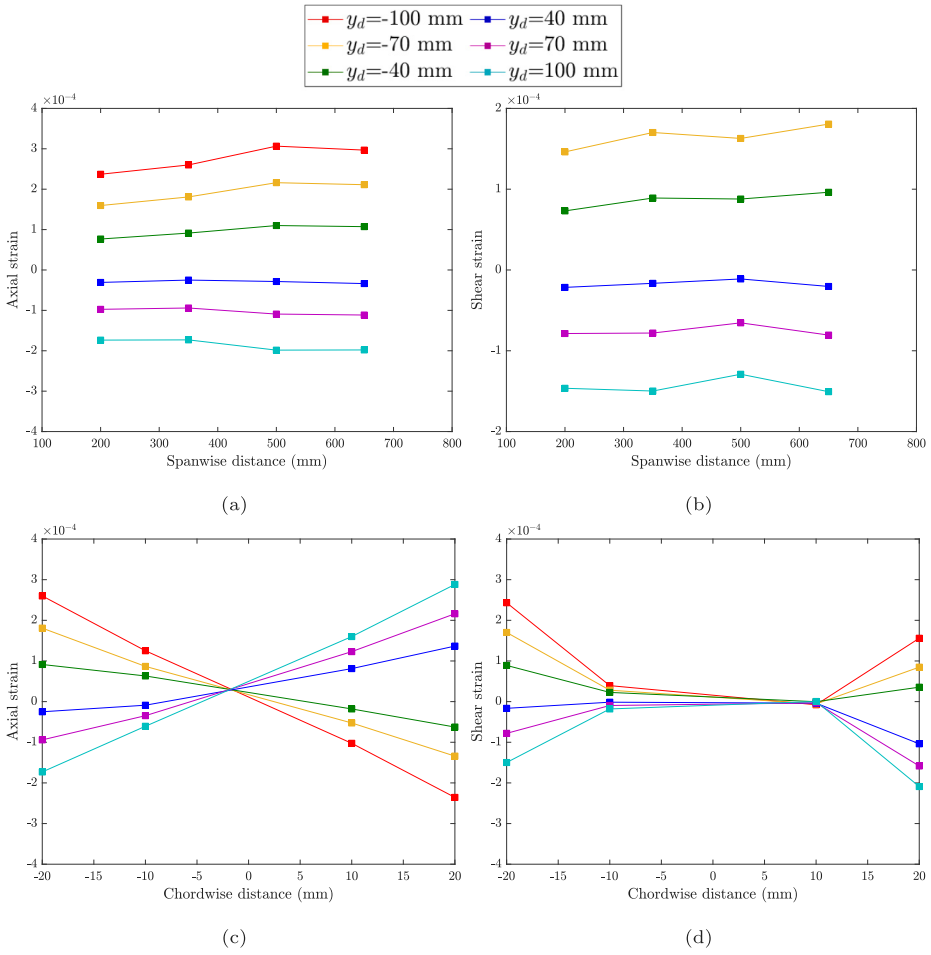

Fig. 21. Distribution of axial and shear strain along the spanwise and chordwise direction of the 20° spar subjected to a loading of 20 kg placed at varies chordwise positions.

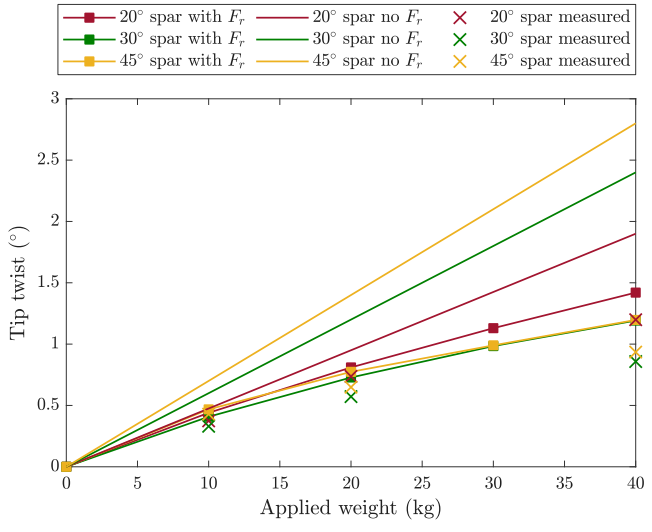

Fig. 22. Comparison of the tip twist of the spars with and without the restoring forces.

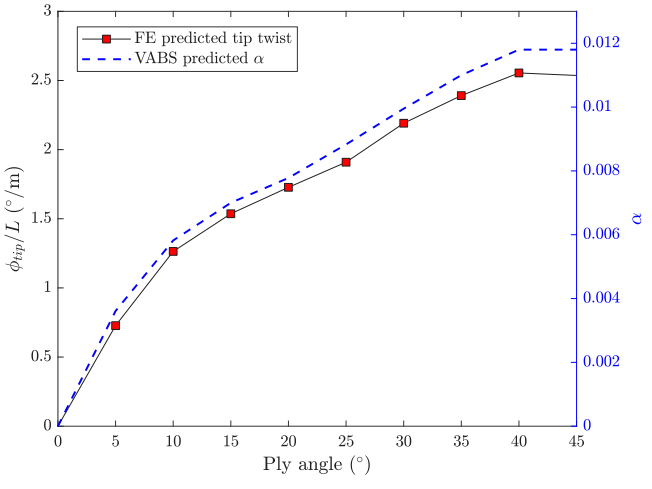

Fig. 23. Comparison of the tip twist of the spars without the restoring forces and VABS predicted α.

References

[1] Barbarino S, Bilgen O, Ajaj R M, Friswell M I, Inman D J. A review of morphing aircraft. J Intell Mater Syst Struct 2011;22(9):823–77.

[2] Li D, Zhao S, Ronch A D, Xiang J, Drofelnik J, Li Y, Zhang L, Wu Y, Kintscher M, Monner H P, Rudenko A, Guo S, Yin W, Kirn J, Storm S, Breuker R D. A review of modelling and analysis of morphing wings. Prog Aerosp Sci 2018;100:46–62.

[3] Fincham JHS, Friswell MI. Aerodynamic optimisation of a camber morphing aerofoil. Aerosp Sci Technol 2015;27:245–55.

[4] Gu Huaiyuan, Amoozgar Mohammadreza, Shaw Alexander D, Zhang Jiaying, Wang Chen, Friswell Michael I. Experimental study of lag-twist coupling concept for rotor blade application. Compos Struct 2021.

[5] Amoozgar M R, Shaw A D, Zhang J, Friswell M I. Composite blade twist modification by using a moving mass and stiffness tailoring. AIAA J 2019;57:4218–25.

[6] Amoozgar MR, Shaw AD, Zhang J, Friswell MI. The effect of a movable mass on the aeroelastic stability of composite hingeless rotor blades in hover. J Fluids Struct 2019;87:124–36.

[7] Gibbs Y. NASA Armstrong fact sheet: X-29 advanced technology demonstrator aircraft. National Aeronautics and Space Administration; 2017.

[8] Motley M R, Barber R B. Study on composite bend-twist coupled wind turbine blade for passive load mitigation. Compos Struct 2019;213:173–89.

[9] Stäblein Alexander R. Analysis and design of bend-twist coupled wind turbine blades. In: MARE-WINT: New materials and reliability in offshore wind turbine technology. Springer International Publishing; 2016, p. 67–80.

[10] Perron Sebastien Gauthier, Drela Mark. Passive gust load alleviation through bend-twist coupling of composite beams on typical commercial airplane wings. In: 54th AIAA/ASME/ASCE/AHS/ASC structures, structural dynamics, and materials conference. http://dx.doi.org/10.2514/6.2013-1490.

[11] Meng Hang, Lien Fue-Sang, Glinka Gregory, Geiger Paul. Study on fatigue life of bend-twist coupling wind turbine blade based on anisotropic beam model and stress-based fatigue analysis method. Compos Struct 2019;208:678–701.

[12] Liu Zhanke, Young Yin L. Utilization of bend–twist coupling for performance enhancement of composite marine propellers. J Fluids Struct 2009;25(6):1102–16.

[13] Rohde S E, Ifju P G, Sankar B V, Jenkins D A. Experimental testing of bend-twist coupled composite shafts. Exp Mech 2015;55:1613–25.

[14] Chandra R, Stemple A D, Chopra I. Thin-walled composite beams under bending, torsional, and extensional loads. J Aircr 1990;27:619–26.

[15] Gu H, Shaw A D, M. Amoozgarb J Zhang, Wang C, Friswell M I. Twist morphing of a composite rotor blade using a novel metamaterial. Compos Struct 2020. (In press).

[16] Lobitz D W, Veers P. Aeroelastic behavior of twist-coupled HAWT blades. ASME Wind Energy Symp 1998;21:17–24.

[17] Sun J, Guan Q, Liu Y, Leng J. Morphing aircraft based on smart mater struct: A state-of-the-art review. J Intell Mater Syst Struct 2016;27:2289–312.

[18] Ermakova A, Dayyani I. Shape morphing of aircraft wing: Status and challenges. Mater Des 2010;31:1284–92.

[19] Abdullah E, Bil C, Watkins S. Application of smart materials for adaptive airfoil shape control. In: 47th AIAA aerospace sciences meeting including the new horizons forum and aerospace exposition; 2009.

[20] Barbarino S, Flores E I Saavedra, Ajaj R M, Dayyani I, Friswell M I. A review on shape memory alloys with applications to morphing aircraft. Smart Mater Struct 2014;23.

[21] Lagoudas Dimitris C. Modeling and engineering applications. In: Shape Memory Alloys. Springer US; 2008.

[22] Ameduri S, Concilio A. A shape memory alloy torsion actuator for static blade twist. J Intell Mater Syst Struct 2019;30:2605–26.

[23] Bhattacharyya A, Lagoudas D C, Wang Y, Kinra V K. On the role of thermoelectric heat transfer in the design of SMA actuators: theoretical modeling and experiment. Smart Mater Struct 1995;4:252–63.

[24] Chopra I. Review of state of art of smart structures and integrated systems. AIAA 2002;40:2145–87.

[25] Chen P C, Chopra I. Induced strain actuation of composite beams and rotor blades with embedded piezoceramic elements. Smart Mater Struct 1996;5:35–48.

[26] Mukherjee A, Varughese B. Design guidelines for ply drop-off in laminated composite structures. Compos Part B Eng 2001;32:153–64.

[27] Cesnik CE S, Hodges D H. VABS: A New concept for composite rotor blade cross-sectional modeling. J Am Helicopter Soc 1997;42:27–38.

[28] Yu W, Hodges D H. Generalized Timoshenko theory of the variational asymptotic beam sectional analysis. J Am Helicopter Soc 2005;50:46–55.